19e Journées de l'Hydrodynamique
26 – 28 novembre 2024, Nantes

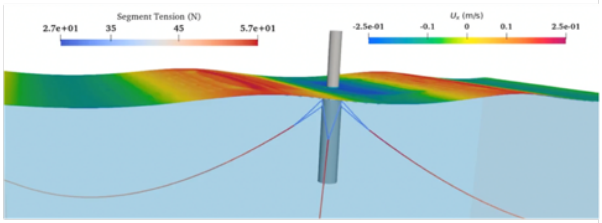

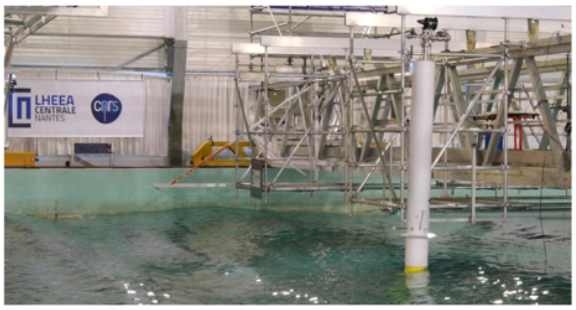

PERFECT ABSORPTION OF BOAT WAKE USING A MICROSTRUCTURED WALL

Adam ANGLART[(1)], Samantha KUCHER[(1)]
Philippe PETITJEANS[(1)], Agnès MAUREL[(2)], Vincent PAGNEUX[(3)]
adam.anglart@espci.fr

[(1)]PMMH, ESPCI Paris, Université PSL, Sorbonne Université, CNRS, 75005 Paris
[(2)]Institut Langevin, ESPCI Paris, Université PSL, CNRS, 75005 Paris
[(3)]LAUM, Le Mans Université, CNRS, 72085 Le Mans

Summary

Absorption plays a crucial role in wave control, with broad applications ranging from noise reduction in acoustics to coastal protection and energy harvesting from water waves. Numerous methodologies have been proposed, often relying on resonant mechanisms. A particularly effective approach for achieving perfect absorption is through critical coupling, wherein resonance leakages balance with inherent system losses, resulting in peak absorption.

Understanding and engineering devices using critical coupling involves examining the complex frequency plane. By strategically manipulating resonator geometries, it is possible to shift the reflection coefficient zeros in the complex frequency plane to the real axis, thereby achieving perfect absorption.

In the context of water waves, this strategy can be applied to create perfect absorbers using subwavelength resonators. This entails aligning radiation damping with the intrinsic viscous damping of the resonators. In this work, we have developed and implemented a microstructured vertical wall made of resonant cavities capable of achieving perfect absorption. The microstructured wall allows for almost full absorption of the wake pattern generated by a moving source, such as a boat. This system appears promising for coastal protection, particularly in areas with lateral confinement, offering practical applications in river engineering.

I – Introduction

Absorption remains a crucial focus within the field of wave manipulation, with applications that span noise mitigation in acoustics, coastal protection, and energy harvesting using water waves. Various approaches have been developed, predominantly leveraging resonant mechanisms [1–11]. Perfect absorption has been also achieved via critical coupling in an acoustic waveguide [12], where broadband absorption was accomplished using a subwavelength scatterer constructed from a viscoelastic porous plate.

The concept of critical coupling can be analyzed and applied using the complex frequency plane [13]. Critical coupling, which involves balancing the resonance leakages with inherent losses of the system, produces a peak in absorption. By carefully adjusting the geometric parameters of resonators, the reflection coefficient's zeros in the complex frequency plane can be shifted onto the real axis, thus achieving perfect absorption.

In the context of water waves, this principle has been applied to design a perfect absorber comprising a subwavelength resonator. In [14], the experiments were conducted within a waveguide featuring an off-centered open cavity at one end, where nonlinear wave interactions and resonator geometry were used to equate radiation damping with viscous losses.

This paper aims to extend this concept to mitigate the reflection of boat wakes generated near shorelines. Such a system holds significant potential for coastal protection, particularly in scenarios involving lateral confinement, making it directly applicable to river engineering [15–18]. Boat wakes are characterized by their iconic V-shape produced when a vessel travels at a constant speed in a straight line. They have been widely studied since Kelvin's foundational work on the wake angle [19]. Recent research on boat wakes continues to explore factors like water depth and boat geometry [20–23].

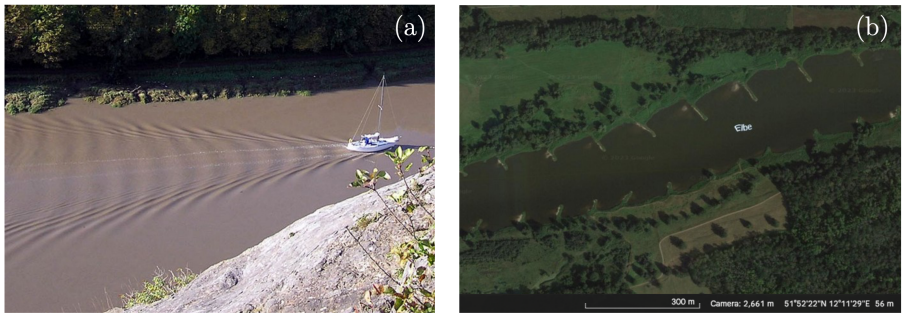

Figure 1: (a) Boat wake in the Avon Gorge, England [24]. (b) Groynes in Elbe river, Germany (Google Earth).

It is noteworthy that structures similar to those proposed for boat wake absorption are already utilized for erosion control, such as groynes, which are angled to deflect flow rather than absorb wave energy [25–27]. Figure 1 illustrates *groynes* constructed along the Elbe River in Germany. While visually resembling our experimental setup, these structures aim to manage sediment movement rather than wave absorption. Their use in rivers, however, demonstrates the feasibility of implementing such systems in practical scenarios.

In this work, we begin by introducing the effective boundary condition that replaces the solid wall, demonstrating that this configuration facilitates the existence of surface modes characterized by evanescent waves propagating away from the microstructured

wall. Next, we analyze the oblique incidence of a plane wave on this wall, comparing reflection coefficients obtained through a multimodal method with those derived from the effective boundary condition. By employing the complex frequency plane, we identify a resonance within this setup that has the potential to create a perfectly absorbing boundary. Therefore, we propose an experimental design in which a boat moves parallel to a microstructured wall (grating), allowing for the absorption of the boat wake and significantly diminishing its reflection on the walls.

II – Microstructured wall (grating)

II – 1 Effective boundary condition

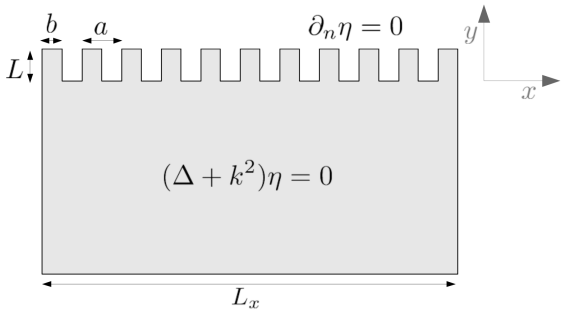

Figure 2: Geometry of the periodic grating of periodicity a, filling ratio b and length L.

We begin our analysis by examining the modes within a closed cavity, one of whose walls is constructed from a periodic arrangement of rectangular inclusions, characterized by a periodicity a, a width b, and a length L, as depicted in Figure 2. For this study, we assume a time-harmonic dependence represented by $e^{-i\omega t}$. The governing equation for the surface elevation field $\eta(x, y)$ is described by the Helmholtz equation

$$(\Delta + k^2)\eta(x, y) = 0, \tag{1}$$

where k denotes the wavenumber, and we apply Neumann boundary conditions at the cavity walls ($\partial_n\eta = 0$). If the periodicity a of the grating is significantly smaller than the wavelength $\lambda = 2\pi/k$, we assume that each cavity supports only a single propagating mode, leading to the mono-modal condition

$$\frac{\partial^2\eta}{\partial y^2} + k^2\eta = 0, \tag{2}$$

The solution to this equation can be expressed as $\eta = A\cos[k(y - L)]$, which fulfills the Neumann boundary condition at $y = L$. At the lower interface of the cavity, defined as $y = 0$ (denoted as $y = 0^-$), we have

$$\frac{\partial\eta}{\partial y} = k\tan(kL)\eta. \tag{3}$$

Next, we enforce the continuity conditions for the field and its derivative at the interface $y = 0$

$$\eta(0^-) = \eta(0^+), \quad a\frac{\partial \eta}{\partial y}(0^-) = b\frac{\partial \eta}{\partial y}(0^+). \tag{4}$$

Combining equations (3) and (4) at $y = 0^-$, we derive:

$$\frac{\partial \eta}{\partial y} = \frac{b}{a}k\tan(kL)\eta, \tag{5}$$

where we define $\gamma = \frac{b}{a}k\tan(kL)$. We then seek a general solution $\eta(x, y)$ in the region where $y < 0$ (external to the microstructure) and propose the form $\eta(x, y) = e^{iqx}f(y)$ which must satisfy the Helmholtz equation. This leads us to

$$f'' + (k^2 - q^2)f = 0. \tag{6}$$

In this work, we focus on the absorption characteristics of the microstructure, particularly interested in modes that remain localized near the grating, referred to as surface modes (evanescent waves). These modes can be expressed as $f(y) = e^{\gamma y}$, which decay for $y < 0$ with a wavenumber γ. Substituting this form into equation (6) gives us $k^2 - q^2 = -\gamma^2$. Thus, the dispersion relation can be expressed as [11]

$$q^2 = \left[\left(\frac{b}{a}\tan(kL)\right)^2 + 1\right]k^2. \tag{7}$$

The primary focus of this investigation is the interaction between a boat wake and the grating. In practical experiments, we must consider energy losses; incorporating a small imaginary component into the wave vector implies that these surface modes become less apparent. Given that the theoretical framework suggests the existence of surface modes, we will now turn our attention to a related problem: the incidence of a plane wave on a microstructured wall.

II – 2 Plane wave incidence on a microstructured wall

II – 2.1 Reflection coefficient

We now examine the incidence of a plane wave on a microstructured wall, depicted in Figure 3a, and address the problem using the multimodal method [10, 11]. Assuming time-harmonic dependence $e^{-i\omega t}$, we consider a plane wave with wavenumber k and angle θ incident on an infinite grating with periodicity a. Each cavity has a length L and width b. The system is governed by the Helmholtz equation (1) with Neumann boundary conditions on the wall surface, $\partial_n \eta = 0$, and Floquet periodic boundary conditions in the x-direction. We define the region outside the grating as Region 1 and inside the grating as Region 2. The solution in these regions can be expressed as

$$\begin{aligned}
\eta^{(1)}(x, y) &= e^{ik_y y}\phi_0^{(1)}(x) + \sum_{n=-\infty}^{+\infty} R_n e^{-i\alpha_n y}\phi_n^{(1)}(x) \\
\eta^{(2)}(x, y) &= \sum_{n=0}^{+\infty} A_n \cos\left(\zeta_n(y - L)\right)\phi_n^{(2)}(x)
\end{aligned} \tag{8}$$

where the transverse functions $\phi_n^{(1)}(x) = \frac{1}{\sqrt{a}}e^{i\beta_n x}$ and $\phi_n^{(2)}(x) = \sqrt{\frac{2-\delta_{n0}}{b}}\cos(\gamma_n x)$, satisfy the periodic and Neumann boundary conditions in Regions 1 and 2, respectively. The

wavenumbers are defined as $\beta_n = k_x + 2\pi n/a$, $\gamma_n = n\pi/b$, $\alpha_n = \sqrt{k^2 - \beta_n^2}$, and $\zeta_n = \sqrt{k^2 - \gamma_n^2}$, with $k_x = k\sin\theta$ and $k_y = k\cos\theta$ as the projections of the incident wave vector.

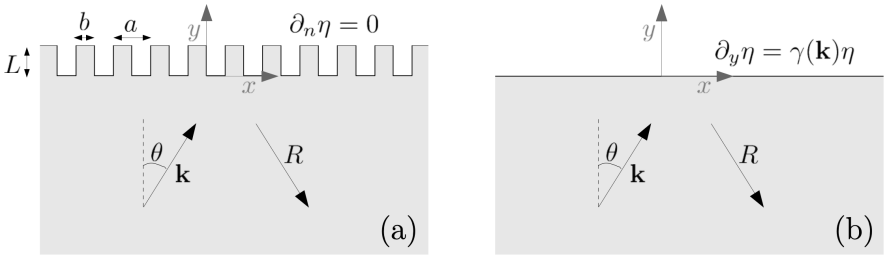

Figure 3: (a) Geometry of the infinite periodic grating with periodicity a, filling ratio b, and cavity length L. (b) Equivalent geometry with an effective boundary condition substituting the microstructured wall. A plane wave with wavenumber k is incident obliquely at an angle θ, and the specular reflection of the fundamental mode, characterized by reflection coefficient R, is indicated.

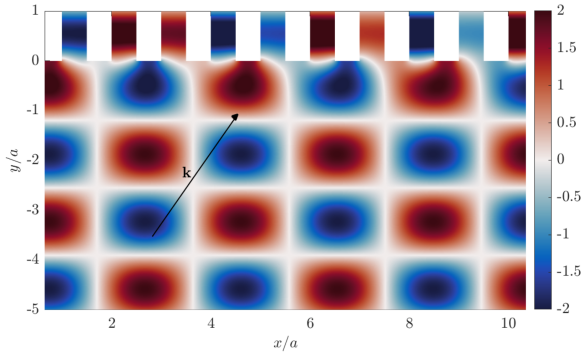

Figure 4: Numerical result: Real part of the field $\eta(x, y)$ produced by the incidence of a plane wave with $ka = 9\pi/10$ and $\theta = 35°$ on a grating characterized by $b/a = 0.5$ and $L/a = 1$.

The reflection coefficient R_n and the complex amplitude A_n represent the modes in region 2. The quantities k_x and k_y correspond to the projections of the incident wavenumber on the x and y axes, respectively: $k_x = k\sin\theta$ and $k_y = k\cos\theta$. It is important to note that in region 1, the transverse functions $\phi_n^{(1)}$ are a-periodic, while in region 2, the transverse functions $\phi_n^{(2)}$ satisfy Neumann boundary conditions at the lateral walls.

Next, we examine the scenario depicted in Figure 3b, where the grating is replaced by an effective boundary condition as defined by Eq. (5). Focusing on specular reflection, we define the reflection coefficient for the fundamental mode as $R = R_0$. The corresponding solution is

$$\eta(x, y) = e^{i(k_x x + k_y y)} + Re^{i(k_x x - k_y y)}. \tag{9}$$

By applying the effective boundary condition (5), we obtain

$$\left.\frac{\partial \eta}{\partial y}\right|_{y=0} = ik_y e^{ik_x x} - ik_y R e^{ik_x x} = \gamma(e^{ik_x x} + Re^{ik_x x}), \tag{10}$$

which allows for the determination of the reflection coefficient

$$R = \frac{ik_y - \gamma}{ik_y + \gamma}. \tag{11}$$

For real values of k, it follows that $|R| = 1$, in accordance with energy conservation. Consequently, to analyze the system's behavior, we focus on the phase of the complex reflection coefficient R. Figure 5 compares the phase of R obtained using the modal method with the phase derived from Eq. (11), for varying ratios of b/a and different cavity depths L. We vary the frequency within the range $ka \in [0, \pi]$, where $ka = \pi$ represents the lowest cutoff frequency of the system (corresponding to $\theta = \pi/2$).

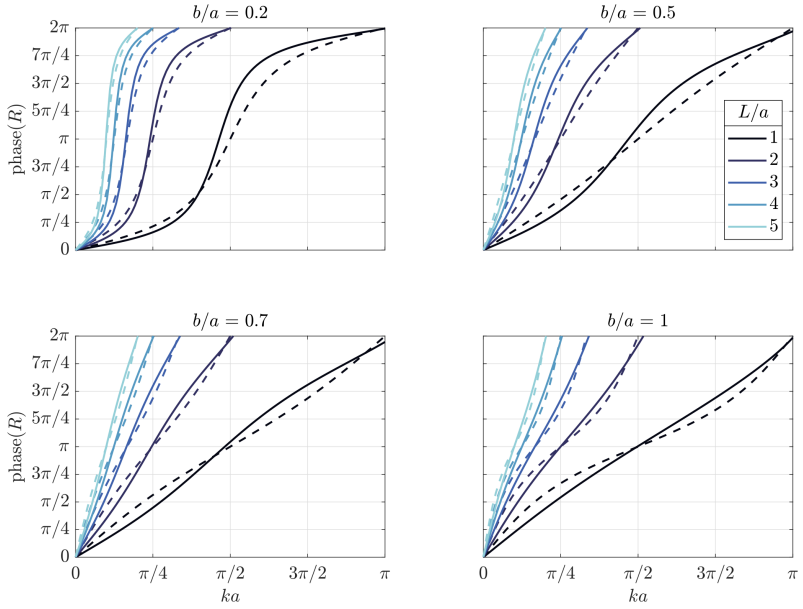

Figure 5: Theoretical and numerical results: Phase of the reflection coefficient as a function of ka, for different ratios b/a and L/a. The solid lines correspond to the multimodal method calculation, while the dashed lines are obtained from the reflection coefficient given by Eq. (11), calculated using the effective boundary condition in Eq. (5).

As expected, the two curves show slight discrepancies due to the approximations used in the effective boundary condition (dashed lines). Additionally, a resonance appears, becoming more pronounced as the b/a ratio decreases and the cavity depth L increases, particularly for long, narrow cavities.

II – 2.2 Resonance of the grating

We begin by considering Eq. (11), which describes the reflection coefficient in the complex frequency plane and can be rewritten as

$$R = \frac{\cot(kL) + i\frac{b}{a\cos\theta}}{\cot(kL) - i\frac{b}{a\cos\theta}}. \tag{12}$$

The poles and zeros are located at $\cot(kL) - i\frac{b}{a\cos\theta} = 0$ and $\cot(kL) + i\frac{b}{a\cos\theta} = 0$, respectively. These values are complex conjugates: the poles have a negative imaginary part and the zeros a positive imaginary part. This behavior is typical for complex resonance

frequencies [28] and is independent of the mono-mode approximation used for the wave propagation towards infinity. Near the pole-zero pair, the reflection coefficient can be approximated as

$$R = \frac{kL - \frac{\pi}{2} - i\frac{b}{a\cos\theta}}{kL - \frac{\pi}{2} + i\frac{b}{a\cos\theta}}. \tag{13}$$

For a pole $K_R = k_R - i\alpha_R$, where $k_R = \pi/2$ is the real part of the resonance frequency and $\alpha_R = \frac{b}{a\cos\theta}$, the reflection coefficient near the resonance frequency is given by

$$R = e^{i\varphi}\frac{k - k_R - i\alpha_R}{k - k_R + i\alpha_R}. \tag{14}$$

Here, φ represents a slowly varying phase that captures the gradual variation of R in contrast to the rapid fluctuations near the resonance. For real values of k, φ is real, and energy conservation is satisfied, i.e., $|R| = 1$.

To obtain the complex resonance frequency, we consider a plane wave incidence at an angle $\theta = 35°$ and use the multimodal method to calculate the reflection coefficient R_0. We then fit the data using Eq. (14), with initial guesses for the real and imaginary parts of the pole. The results are shown in Figure 6a, for a configuration with $L/a = 1$ and $b/a = 0.2$. Additionally, the phase of R calculated using the effective boundary condition is compared with the fit from Eq. (14). This procedure is repeated for different cavity widths (varying b/a), and the resulting data is plotted in Figure 6b.

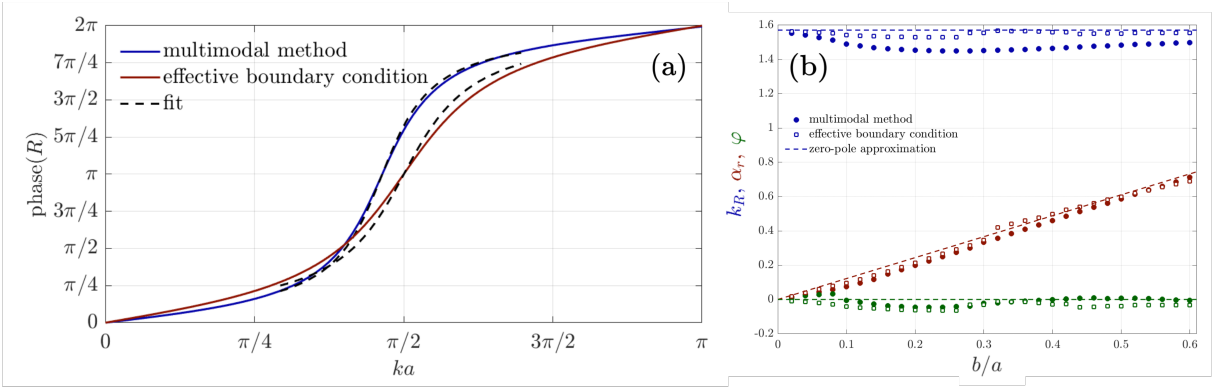

Figure 6: (a) Phase of the reflection coefficient R as a function of ka for $L/a = 1$ and $b/a = 0.2$. The blue line represents the reflection coefficient calculated using the multimodal method, while the red line shows the result from Eq. (12). Dashed lines indicate the fit near the resonance frequency using Eq. (14). (b) Complex resonance frequencies for various b/a configurations with fixed $L/a = 1$. The parameters k_R, α_R, and φ are obtained by fitting R with Eq. (14). Dots indicate values from fitting the multimodal method, squares represent the fit from Eq. (12), and dashed lines correspond to the zero-pole approximation from Eq. (13), with $k_R = \pi/2$, $\alpha_R = \frac{b}{a\cos\theta}$, and $\varphi = 0$. A plane wave incidence at $\theta = 35°$ is assumed.

We observe that the real part of the resonance frequency remains largely constant around $k_R \approx \pi/2$, corresponding to the $\lambda/4$ resonance, for both the modal and effective boundary condition methods. However, the imaginary part exhibits significant variation, becoming more leaky as the cavity width increases. This suggests that adjusting the cavity width allows tuning of wave leakage. The phase φ is approximately constant but

slowly varies with b/a, which helps explain the discrepancy between the phase of R and its fit in Figure 6a. As expected, the effective boundary condition results are closer to those predicted by Eq. (13).

To account for intrinsic losses, we introduce a viscous damping term α_v by shifting the imaginary part of the resonance frequency as $k \to k + i\alpha_v$. The reflection coefficient becomes

$$R = e^{i\varphi} \frac{k - k_R - i(\alpha_R - \alpha_v)}{k - k_R + i(\alpha_R + \alpha_v)}. \tag{15}$$

Setting $\alpha_v = \alpha_R$ results in perfect absorption, as the poles and zeros shift downwards in the imaginary axis, as shown in Figure 7. This corresponds to the zeros crossing the real axis, indicating perfect absorption. This approach is similar to the one used in [14], where a waveguide with a resonator at the end has been used, combining quarter-wavelength and Helmholtz resonator mechanisms. In contrast, we analyze the interaction of an oblique plane wave with an infinite periodic medium made of rectangular cavities acting as an absorbing wall.

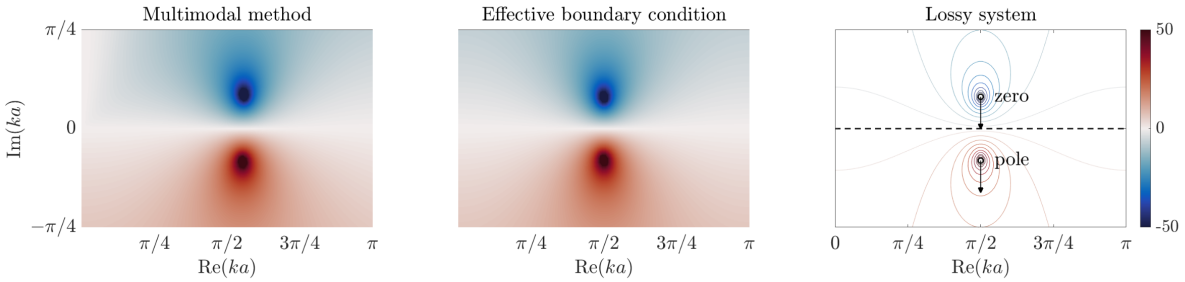

Figure 7: Representation of $20\log(|R|)$ in the complex frequency plane. (a) Reflection coefficient computed using the multimodal method. (b) Reflection coefficient derived from Eq. (12). (c) Contour plot showing the position of the zero and pole of R obtained with the effective boundary condition (Eq. (12)), illustrating the shift in the pole and zero positions when losses are introduced into the system.

III – Experimental setup

Experiments were conducted in a water tank with dimensions 1.77 m × 0.60 m, exploring water depths within the range $h \in [0.02, 0.09]$ m. The Fourier Transform Profilometry (FTP) method, was utilized to measure free surface deformations using a high-speed camera (Photron FASTCAM Mini WX100) and a video projector (EPSON EH-TW9200W), both aligned in a parallel-axis setup. The camera and projector were positioned $D = 0.45$ m apart and located at a height $L_p = 1.88$ m above the water level, achieving a spatial resolution of 0.28 mm/px with a frame rate of 125 fps.

The wake was generated by a partially submerged spherical object (referred to as the "boat") with a 4.2 cm diameter. At the water surface, the object's cross-section diameter was reduced to 3.7 cm. Placed 17.5 cm from the wall, the boat was mounted on a motorized platform that moved at a uniform speed U, controlled by an Arduino-driven stepper motor. This setup minimized shadowing effects, especially in the region of interest, as shown in Figure 8.

To characterize the wake, we introduced the Froude number, $\mathrm{Fr} = U/\sqrt{gh}$, where g represents gravitational acceleration and h is the water depth. The dispersion relation for a moving source is expressed as

$$\Omega(\mathbf{k}) = \sqrt{g|\mathbf{k}|\tanh(|\mathbf{k}|h)} - \mathbf{U}\cdot\mathbf{k} \tag{16}$$

where $\mathbf{k}$ is the wavenumber vector with magnitude $k = |\mathbf{k}|$.

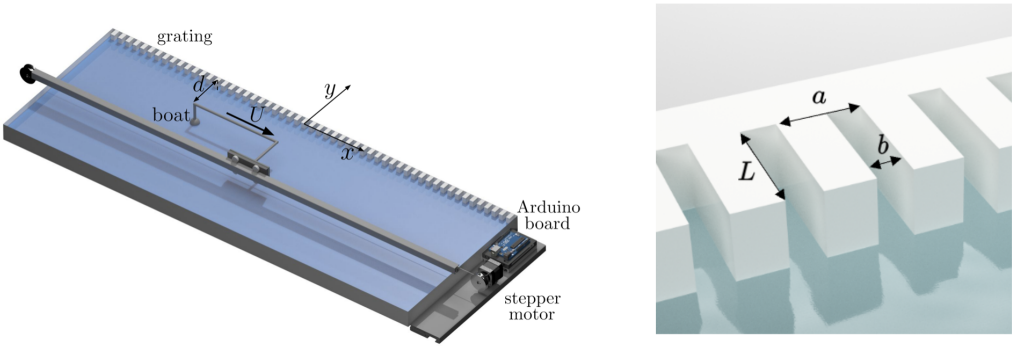

Figure 8: (left) Schematic of the experimental setup. The boat, a partially submerged sphere, is attached to a mobile platform near a microstructured grating wall. The platform moves along a rail at a constant speed U, controlled by an Arduino and stepper motor. The camera and projector, separated by distance D and positioned at height L_p above the water, capture free surface deformations using Fourier Transform Profilometry (FTP). (right) Schematic of the microstructured wall (grating) of periodicity a, width b and length L.

IV – Experimental results

The wavefield data were recorded over time and then averaged with respect to the boat's motion to enhance the resolution of the wake pattern. However, quantifying the reflection of the boat wake is not straightforward. The reflection coefficient is defined for monochromatic waves, but in the case of a boat wake, multiple wavelengths are present. Additionally, the boat's movement changes its position continuously, meaning the waves reaching the wall in a fixed reference frame differ from those moving away. The boat's motion further complicates the analysis by preventing a temporal Fourier transform to isolate a single frequency. Hence, we attempt to quantify the reflection of the boat wake using 2D spatial Fourier transform (2D FFT) which is applied to the section of the wavefield near the wall. The resulting spectra are presented in Figure 9. These spectra reveal a dominant wavenumber $\mathbf{k}$, which varies with the boat's speed, represented by different Fr values.

In Figure 9, we compare the wavefield amplitude profiles for two Froude numbers, $\mathrm{Fr} = 0.54$ (high absorption) and $\mathrm{Fr} = 0.87$ (low absorption), with both the wall and grating configurations. The dashed lines represent the theoretical dispersion relation from Eq. 16. Profiles of the amplitude along the dispersion relation were then used to compute a reflection coefficient $R = \tilde{\eta}_{\mathrm{grating}}/\tilde{\eta}_{\mathrm{wall}}$, comparing the grating's response to that of the wall.

For each Froude number, the reflection coefficient R is plotted as a function of the dominant wavenumber k, as illustrated in Figure 10. This analysis indicates that the

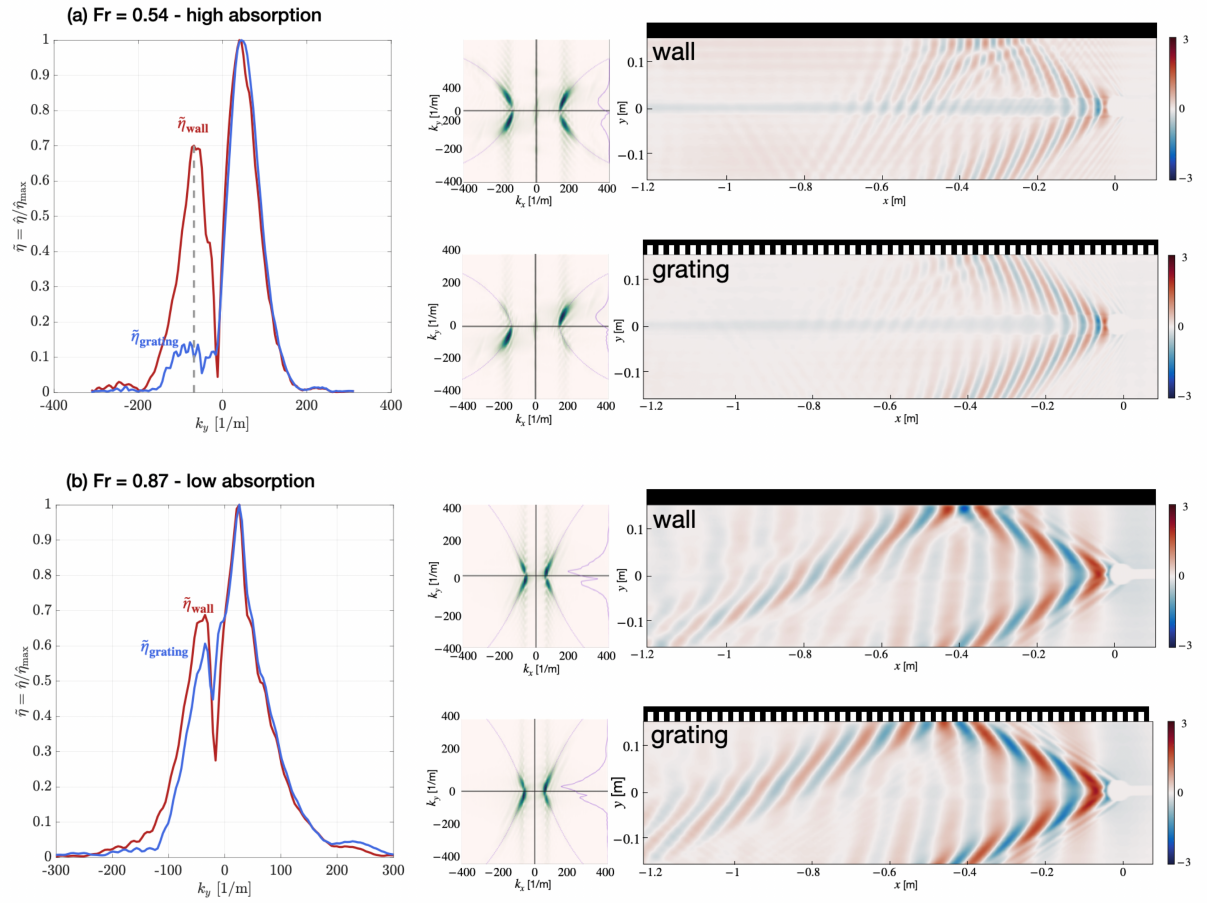

Figure 9: Wavefields with corresponding spectra for two Froude numbers: (a) Fr = 0.54 (high absorption) and (b) Fr = 0.87 (low absorption), showing the amplitude distribution in both wall and grating configurations. Dashed lines on top of the 2D FFT spatial spectra denote the theoretical dispersion relation as described in Eq. 16. The spectra illustrate the dominant wavenumber regions for each configuration, which vary according to the boat's velocity.

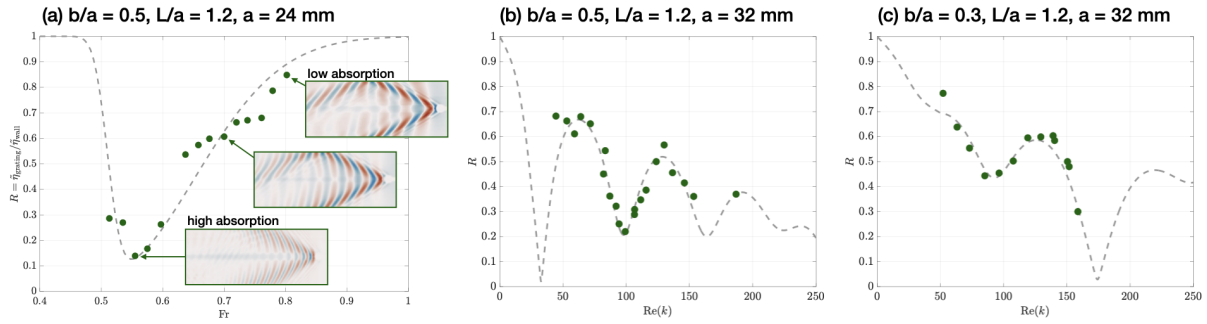

Figure 10: Reflection coefficient $R = \tilde{\eta}_{\text{grating}}/\tilde{\eta}_{\text{wall}}$ as a function of Froude number (Fr) and wavenumber magnitude k. Dashed lines indicate a tentative fit based on Eq. 15, demonstrating a good match with experimental data, albeit not directly derived from this relation.

absorption properties of the grating depend on both Fr and k, with higher absorption observed at lower reflection coefficient values. The experimental data was fitted tentatively using Eq. 15 (dashed lines). Although this fitting is not an exact application of Eq. 15, it demonstrates a reasonable match with the experimental results.

V – Conclusion

This study demonstrates the effectiveness of a microstructured grating wall in absorbing the wake generated by a moving source, such as a boat. Using a combination of theoretical, numerical, and experimental methods, we analyzed wave interactions with the grating wall, focusing on effective boundary conditions, modal analysis, and resonance effects.

An effective boundary condition was established to model the grating as a medium supporting surface modes, which confine wave energy near the wall. This provided initial insights, while a more detailed multimodal analysis enabled calculation of reflection coefficients for different grating configurations. We observed that certain configurations promote resonance, enhancing absorption through critical coupling by aligning poles and zeros in the complex frequency plane.

Experimentally, varying the Froude number allowed us to control the boat wake and measure the resulting wavefields. Results showed that the grating's reflection coefficient, defined as $R = \tilde{\eta}_{\text{grating}}/\tilde{\eta}_{\text{wall}}$, decreases around the designed frequency and nearby frequencies, indicating higher absorption under these conditions. The absorption is achieved by fine-tuning the cavity leakages with viscous losses, resulting in broader, less pronounced resonances, which potentially enables absorption over a range of wavelengths.

In summary, our microstructured wall effectively absorbs wave energy at the designed frequency and neighboring frequencies, suggesting applications in coastal protection by reducing wave reflections in confined environments. Ongoing work optimizes the grating design to enhance absorption across an even broader range of conditions, expanding its potential for practical wave management.

References

[1] Ben Wilks, Fabien Montiel, and Sarah Wakes. Rainbow reflection and broadband energy absorption of water waves by graded arrays of vertical barriers. *Journal of Fluid Mechanics*, 941:A26, 2022.

[2] K Budar and Johannes Falnes. A resonant point absorber of ocean-wave power. *Nature*, 256(5517):478–479, 1975.

[3] DV Evans. A theory for wave-power absorption by oscillating bodies. *Journal of Fluid Mechanics*, 77(1):1–25, 1976.

[4] Sichao Qu and Ping Sheng. Microwave and acoustic absorption metamaterials. *Physical Review Applied*, 17(4):047001, 2022.

[5] Nathan I Landy, Soji Sajuyigbe, Jack J Mock, David R Smith, and Willie J Padilla. Perfect metamaterial absorber. *Physical Review Letters*, 100(20):207402, 2008.

[6] David V Evans and Richard Porter. Wave energy extraction by coupled resonant absorbers. *Philosophical Transactions of the Royal Society A: Mathematical, Physical and Engineering Sciences*, 370(1959):315–344, 2012.

[7] Noé Jiménez, Vicent Romero-García, Vincent Pagneux, and Jean-Philippe Groby. Rainbow-trapping absorbers: Broadband, perfect and asymmetric sound absorption by subwavelength panels for transmission problems. *Scientific Reports*, 7(1):13595, 2017.

[8] Adam Anglart. *Experimental study and modeling of metamaterials for water surface waves.* PhD thesis, Université Paris sciences et lettres, 2021.

[9] Adam Anglart, Agnès Maurel, Philippe Petitjeans, and Vincent Pagneux. Regular sloshing modes in irregular cavities using metabathymetry. *arXiv preprint arXiv:2406.04748*, 2024.

[10] Samantha Kucher, A Koźluk, Philippe Petitjeans, Agnès Maurel, and Vincent Pagneux. Backscattering reduction in a sharply bent water wave channel. *Physical Review B*, 108(21):214311, 2023.

[11] Samantha Kucher. *Control of water waves propagation by micro-architectured materials*. PhD thesis, Université Paris sciences et lettres, 2023.

[12] Vicent Romero-García, Georgios Theocharis, Olivier Richoux, Aurélien Merkel, Vincent Tournat, and Vincent Pagneux. Perfect and broadband acoustic absorption by critically coupled sub-wavelength resonators. *Scientific Reports*, 6(1):19519, 2016.

[13] Vicent Romero-García, Georgios Theocharis, Olivier Richoux, and Vincent Pagneux. Use of complex frequency plane to design broadband and sub-wavelength absorbers. *The Journal of the Acoustical Society of America*, 139(6):3395–3403, 2016.

[14] Eduardo Monsalve, Agnes Maurel, Philippe Petitjeans, and Vincent Pagneux. Perfect absorption of water waves by linear or nonlinear critical coupling. *Applied Physics Letters*, 114(1), 2019.

[15] Zhuo Sun, Zhonglong Chen, Hongtao Hu, and Jianfeng Zheng. Ship interaction in narrow water channels: A two-lane cellular automata approach. *Physica A: Statistical Mechanics and its Applications*, 431:46–51, 2015.

[16] Clément Caplier, Germain Rousseaux, Damien Calluaud, and Laurent David. Effects of finite water depth and lateral confinement on ships wakes and resistance. *Journal of Hydrodynamics*, 32:582–590, 2020.

[17] Claire DeMarco Muscat-Fenech, Tonio Sant, Vito Vasilis Zheku, Diego Villa, and Michele Martelli. A review of ship-to-ship interactions in calm waters. *Journal of Marine Science and Engineering*, 10(12):1856, 2022.

[18] Léo-Paul Euvé, Agnès Maurel, Philippe Petitjeans, and Vincent Pagneux. Asymmetrical wakes over anisotropic bathymetries. *Journal of Fluid Mechanics*, 984:R6, 2024.

[19] Willia Thomson. On ship waves. *Proceedings of the institution of mechanical engineers*, 38(1):409–434, 1887.

[20] Marc Rabaud and Frédéric Moisy. Ship wakes: Kelvin or mach angle? *Physical Review Letters*, 110(21):214503, 2013.

[21] Alexandre Darmon, Michael Benzaquen, and Elie Raphaël. Kelvin wake pattern at large froude numbers. *Journal of Fluid Mechanics*, 738:R3, 2014.

[22] Michael Benzaquen, Alexandre Darmon, and Elie Raphaël. Wake pattern and wave resistance for anisotropic moving disturbances. *Physics of Fluids*, 26(9), 2014.

[23] Ravindra Pethiyagoda, Timothy J Moroney, Christopher J Lustri, and Scott W McCue. Kelvin wake pattern at small froude numbers. *Journal of Fluid Mechanics*, 915:A126, 2021.

[24] Adrian Pingstone. The wake of a slow moving boat, October 2004. Public domain,, via Wikipedia Commons.

[25] Alexander Sukhodolov, Wim SJ Uijttewaal, and Christof Engelhardt. On the correspondence between morphological and hydrodynamical patterns of groyne fields. *Earth Surface Processes and Landforms*, 27(3):289–305, 2002.

[26] B Mohsen, F Ramin, DA Ahmad, and ZA Mirkhalegh. Experimental investigation of local scouring around a series of l-head groynes. *8th ICHE, Nagoya*, pages 383–384, 2008.

[27] Antonios Valsamidis and Dominic E Reeve. A new approach to analytical modelling of groyne fields. *Continental Shelf Research*, 211:104288, 2020.

[28] Vincent Pagneux. Trapped modes and edge resonances in acoustics and elasticity. In *Dynamic Localization Phenomena in Elasticity, Acoustics and Electromagnetism*, pages 181–223. Springer, 2013.